First-principles investigation of the structural and vibrational properties of vitreous $GeSe_2$

Luigi Giacomazzi,[1,2] Carlo Massobrio,[3] and Alfredo Pasquarello[1,2]
[1]*Ecole Polytechnique Fédérale de Lausanne (EPFL), Institute of Theoretical Physics, CH-1015 Lausanne, Switzerland*
[2]*Institut Romand de Recherche Numérique en Physique des Matériaux (IRRMA), CH-1015 Lausanne, Switzerland*
[3]*Institut de Physique et de Chimie des Matériaux de Strasbourg, 23 rue du Loess, Boîte Postale 43, F-67034 Strasbourg Cedex 2, France*
(Received 8 December 2006; published 24 May 2007)

Using a density-functional scheme, we study the structural and vibrational properties of vitreous germanium diselenide (v-$GeSe_2$). Through the use of classical and first-principles molecular-dynamics methods, we generate a set of structural models showing a varying degree of chemical disorder. In particular, two types of structural concepts are represented: one in which the tetrahedral order is preserved to a very large extent, and one which reproduces the high degree of disorder in first-neighbor shells found in first-principles molecular-dynamics simulations of the liquid. The investigated structural properties include the angular distributions, the atomic arrangements in the first-neighbor shells, and the pair-correlation functions. In reciprocal space, we have calculated the x-ray and neutron total structure factors and the partial structure factors. Comparison with experiment gives overall good agreement for the models of either structural conception. We then investigate the vibrational properties via the vibrational density of states and the inelastic neutron spectrum. The considered models yield similar spectra and agree with experimental data. We also obtain infrared and Raman spectra through a density-functional scheme based on the application of finite electric fields. For these spectra, significant differences appear among the models. The comparison with experiment favors a model showing a high degree of chemical order. The Raman intensity is analyzed in terms of the underlying atomic vibrations. The assignment of the Raman companion line to Se motions in edge-sharing tetrahedra is supported.

DOI: 10.1103/PhysRevB.75.174207 PACS number(s): 63.50.+x, 71.15.Mb, 71.23.Cq

I. INTRODUCTION

Vitreous germanium diselenide (v-$GeSe_2$) has been studied extensively as an archetypical material in glass science.[1,2] Despite the similar stoichiometric formula, v-$GeSe_2$ shows a structure very different from that of other AX_2 glasses such as vitreous germania (v-GeO_2) or vitreous silica (v-SiO_2). While v-GeO_2 and v-SiO_2 are well described by random networks of corner-sharing tetrahedra, it has long been established that v-$GeSe_2$ shows in addition a considerable fraction of edge-sharing tetrahedra.[3] More strikingly, due to the close electronegativities of Ge and Se, the atomic structure of v-$GeSe_2$ can depart from chemical order and give rise to homopolar bonds, as shown in recent neutron-diffraction experiments.[4] Moreover, first-principles molecular-dynamics simulations of liquid $GeSe_2$[5,6] have shown the occurrence of a rich variety of structural motifs, including not only homopolar bonds, but also over- and undercoordinated atoms.

Hence, the current theoretical and experimental situation leads to two contending conceptions of the structure of v-$GeSe_2$. To match experimental data,[4] both structural conceptions should account for a small fraction of homopolar bonds. The first conception then corresponds to a structure with strong chemical order, in which the tetrahedral bonding nature of the network is respected to a very large extent, the main distinction with respect to v-GeO_2 and v-SiO_2 being the occurrence of edge-sharing tetrahedra. Model structures of this nature have indeed been generated via classical molecular dynamics.[3] The second conception is based on molecular-dynamics simulations of the liquid which indicate a considerable fraction of nontetrahedral bonding configurations with over- and undercoordinated atoms.[5–7] A quench from the liquid would then give a vitreous structure which preserves these features.[8] Models generated according to either conception generally give structure factors in good agreement with experiment.[3,8,9] Thus diffraction data appear unable to clearly distinguish between the two kinds of atomic structures. It is therefore highly desirable to determine the structure of v-$GeSe_2$ by considering also experimental results other than diffraction data.

Vibrational spectroscopies are widely available and provide a rich body of experimental data which could potentially probe the underlying structure of the vitreous material in a sensitive way. The interpretation of vibrational spectra can be pursued through accurate modeling, as recently demonstrated through the use of a density-functional approach. To date, successful applications concern the vibrational spectra of SiO_2,[10–13] GeO_2,[14,15] and B_2O_3.[16] In these materials, the basic structural units play a primary role in defining the main features in the vibrational spectra. Medium-range structural features, such as intertetrahedral angles and small ring structures, can also be accessed through the analysis of Raman spectra.[12–16] In the case of v-$GeSe_2$, the analysis of the vibrational spectra is expected to be similarly informative. For instance, several studies assign one of the most salient features in the Raman spectrum to edge-sharing tetrahedra.[17–19] A high sensitivity is also expected for homopolar bonding and miscoordinations.

In this paper, we provide a comprehensive analysis of both the structural and vibrational properties of vitreous $GeSe_2$ using a density-functional approach. First, we generate model structures according to the two contending structural conceptions outlined above. For models of either kind of conception, the level of agreement with x-ray[20] and neutron-diffraction data[4,21] is rather similar, confirming the overall weak dependence of this kind of data on the detailed structural arrangements. Then, we address the vibrational

properties and focus on the inelastic neutron, infrared, and Raman spectra for all constructed models. Through the comparison of different models, our investigation highlights the relation between the underlying structural arrangements and the principal features in the vibrational spectra. Furthermore, the comparison with experimental spectra gives insight into the atomic structure of vitreous $GeSe_2$. The generated models show important differences in the calculated vibrational spectra, especially for the infrared and Raman ones. This result indicates that the vibrational spectra can successfully be used to discriminate among models. One of the generated models shows overall good agreement with all the experimental vibrational spectra. The atomic structure of this model clearly favors the conception by which the network structure of v-$GeSe_2$ is mainly chemically ordered. The model that best reproduces the experimental vibrational spectra shows 95% of the Ge atoms in regular tetrahedral units. Moreover, our study provides a clear interpretation of the two principal peaks appearing in the Raman spectrum. In particular, the companion line is assigned to edge-sharing tetrahedra.

This paper is organized as follows. In Sec. II, we describe how we generated our model structures of v-$GeSe_2$. We also describe in this section the technical aspects of our electronic-structure calculations and give the electronic density of states of our model structures. In Sec. III, we address the structural properties of v-$GeSe_2$ focusing on both real-space and reciprocal-space properties, which include the bond-length and bond-angle distributions, the pair-correlation functions, the x-ray and neutron total structure factors, and the partial structure factors. Section IV is devoted to the vibrational density of states, which is analyzed in terms of Ge and Se weights, and then further in terms of rocking, bending, and stretching motions. The inelastic neutron spectrum is calculated and compared to experiment. Section V focuses on infrared properties, such as the dynamical Born charges and the dielectric constants. The dielectric functions are calculated and compared to their experimental counterparts. In Sec. VI, we address the Raman spectra focusing, in particular, on the origin of the dominant Raman doublet and on the role of Se-Se homopolar bonds. The conclusions are drawn in Sec. VII.

II. MODEL GENERATION

We generated three models of vitreous $GeSe_2$. Models I and II are intended to be representative of the structural conception in which a strong chemical order prevails. To obtain these models, we first carried out classical molecular dynamics using the interatomic potentials given by Vashishta *et al.*[3] Through a quench from the melt, we generated disordered structures consisting of chemically ordered networks of corner-sharing tetrahedra, consistent with the literature.[3] The final step of the generation procedure consists in applying a damped first-principles molecular dynamics which further optimizes the structural geometry. The first-principles relaxation only slightly modified the structure achieved by classical molecular dynamics, affecting approximately 10% of the atoms. Typical modifications involve the creation of both over- and undercoordinated atoms. This procedure led to the formation of homopolar Se-Se bonds, but the creation of Ge-Ge bonds was not observed. Other minor modifications involved a slight increase in the equilibrium bond lengths and a corresponding decrease in the intertetrahedral angles. These models contained 180 (model I) and 120 atoms (model II) in a periodically repeated cubic cell, at a density of 4.4 g/cm^3, close to the experimental density of v-$GeSe_2$ (4.2 g/cm^3, Ref. 22).

Model III is representative of the structural conception that the structure in the vitreous state features a rich variety of nearest-neighbor motifs, as found in first-principles molecular-dynamics simulations of liquid $GeSe_2$.[5] To generate model III, we started from a 120-atom configuration of the equilibrated liquid[5,6] by rescaling the coordinates to match the density of the amorphous. We then carried out *ab initio* molecular dynamics at fixed volume, controlling the temperature through Nosé-Hoover thermostats.[23] The liquid was cooled from 1100 to 300 K in three steps. To allow for significant diffusion after the initial change of volume, we evolved the system for 10 ps at 1100 K. This step was followed by runs of 7 and 5 ps at 900 and 600 K, respectively. Then, the temperature was set at 300 K and a long simulation of 22 ps was performed. Because of the continuing structural changes, it was preferred to perform relatively shorter runs at intermediate temperatures in favor of a longer simulation at 300 K. The final structure was obtained from a quench to $T=0$ K.

In the present work, we performed electronic-structure calculations and molecular dynamics using first-principles methodologies,[24,25] as provided in the QUANTUM-ESPRESSO package.[26] The electronic structure was treated within a generalized gradient approximation[27] (GGA) to density-functional theory (DFT). Core-valence interactions were described through norm-conserving pseudopotentials for Ge and Se.[5,28] For the electron wave functions and charge density, we used plane-wave basis sets defined by energy cutoffs of 15 and 120 Ry, respectively.[25] The Brillouin zone was sampled at the Γ point.

We derived the vibrational frequencies and eigenmodes from the dynamical matrix, which was calculated numerically by taking finite differences of the atomic forces.[10] For accessing the infrared and Raman spectra, we took advantage of a recently developed scheme for applying a finite electric field in periodic cell calculations.[29] We obtained the relevant coupling tensors by numerically calculating first and second derivatives of the atomic forces with respect to the electric field.[30] We applied fields of ± 0.0005 a.u. To check the convergence of our finite-difference scheme, we also considered electric fields of $\pm 0.000\,25$ a.u. but found negligible modifications of the calculated vibrational spectra.

We show in Fig. 1(a) the electronic density of states of our three models. Overall, the three models show similar features. The origin of the bands[31] is analogous to the cases of SiO_2 (Ref. 32) and GeO_2 (Ref. 15). The lowest band arises from Se $4s$ states. The low-energy side of the central band results from the Ge-Se bonds, formed by Ge sp^3 and Se $4p$ orbitals. The high-energy side of this central band, which defines the top of the valence band, consists of Se $4p$ lone pairs. The low-energy part of the conduction band mainly

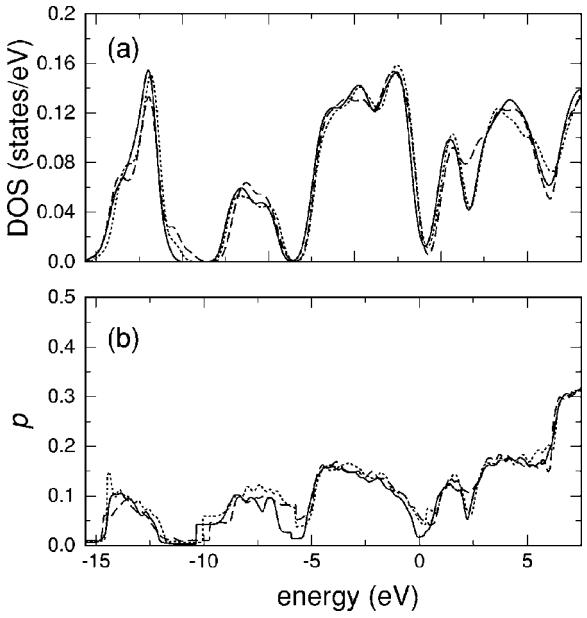

FIG. 1. (a) Electronic density of states (DOS) and (b) participation ratio p of our models of v-$GeSe_2$: model I (solid), model II (dotted), and model III (dashed). The highest occupied states are aligned at 0 eV. Gaussian broadenings of 0.25 and 0.1 eV are used in (a) and (b), respectively.

consists of antibonding states associated with the Ge-Se bond. The present results are consistent with the electronic density of states obtained for v-$GeSe_2$ within an approximate density-functional scheme[8] and with that obtained for model clusters of $GeSe_2$.[31]

The calculated energy separation between the highest occupied and lowest unoccupied Kohn-Sham levels differs among our models. We found band gaps of 0.50, 0.62, and 0.81 eV for models I, II, and III, respectively. These band gaps are all significantly smaller than the experimental optical gap (2.2 eV, Ref. 33). An underestimation of the band gap is usual in density-functional calculations. In the case of disordered systems, an additional difficulty in the comparison with experiment arises because of size limitations that prevent an accurate description of the band tails. Indeed, integration of the density of states between −1.0 and +1.5 eV with respect to the Fermi level gives differences of only ~10% among the models. The similar nature of electronic properties in our models is also confirmed by inspecting the participation ratio [Fig. 1(b)].[34] The three models show similar curves with a participation ratio increasing with Kohn-Sham energy of the eigenstate, as found previously for amorphous SiO_2.[35]

III. STRUCTURAL PROPERTIES

A. Real-space properties

In all our models, the average Ge-Se bond length is found to be slightly larger than the experimental one (see Table I). The bond elongation should be attributed to a general tendency of first-principles GGA calculations.[28] In Fig. 2, we compare the Ge-Se bond-length distributions of our models.

TABLE I. Structural properties of our models of v-$GeSe_2$: number of atoms (N), average Ge-Se-Ge and Se-Ge-Se angles, and average bond length (d_{GeSe}). The respective standard deviations are given in parentheses. The experimental value for the bond length is taken from Ref. 4.

	N	∠ Ge-Se-Ge	∠ Se-Ge-Se	d_{GeSe} (Å)
Model I	180	100.6° (12.1°)	109.1° (9.5°)	2.42 (0.05)
Model II	120	107.8° (12.7°)	108.6° (12.0°)	2.44 (0.07)
Model III	120	100.7° (16.2°)	106.8° (11.3°)	2.47 (0.13)
Expt.				2.36

Model I shows the most narrow distribution with a peak at ~2.4 Å, while models II and III have wider bond-length distributions characterized by tails extending up to 3.0 Å.

The structure of model I mainly shows well defined tetrahedral units with an average Se-Ge-Se angle (109.1°) close to the ideal one and a standard deviation of 9.5°. The structure of model II is also characterized by well defined tetrahedral units, but shows larger distortions presumably due to the smaller model size. In model III, only 78% of the Ge atoms form tetrahedral units and the average Se-Ge-Se angle deviates more significantly from the ideal tetrahedral angle.

We give in Fig. 3 the Ge-Se-Ge angle distributions for the Se atoms twofold coordinated by Ge in our models. For models I and II, this includes a very large fraction of the Se atoms (94% and 86%, respectively), consistent with the chemically ordered nature of these networks (Table II). In model III, this distribution only concerns 55% of the Se atoms (Table II). This model indeed shows a large fraction of Se atoms onefold (21%) or threefold (20%) coordinated by Ge. The average angle in models I and III is about 101° with standard deviations of 12.1° and 16.2°, respectively. In model II, the average angle is slightly larger (107.8°), but shows a similar standard deviation of 12.7°. The parameters characterizing the bond-length and bond-angle distributions of our models are summarized in Table I.

The three Ge-Se-Ge angle distributions in Fig. 3 feature a distinct peak at 80° that corresponds to edge-sharing tetrahedra. Its intensity reflects the concentration of such units in the models and can be quantified in terms of the percentage of involved Ge atoms. For models I, II, and III, this concen-

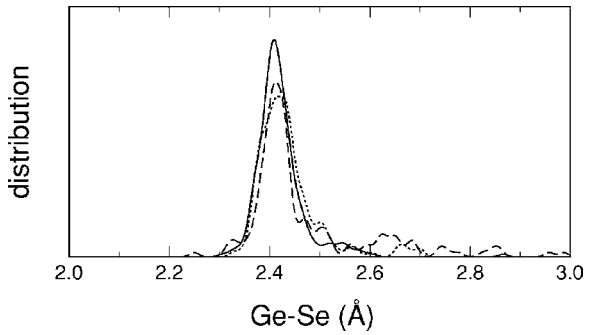

FIG. 2. Distribution of Ge-Se bond lengths in model I (solid), model II (dotted), and model III (dashed). A Gaussian broadening of 0.01 Å is used.

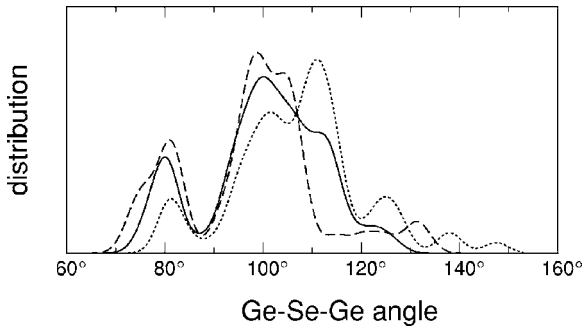

FIG. 3. Distribution of the Ge-Se-Ge intertetrahedral angle for our models of v-$GeSe_2$: model I (solid), model II (dotted), and model III (dashed). A Gaussian broadening of 2.5° is used.

tration amounts to 33%, 15%, and 48%, respectively. The concentration of edge-sharing tetrahedra in model I is very close to the experimental estimate (34%, Ref. 4) and to results previously obtained by Vashishta *et al.* (32%, Ref. 3).

An atomic configuration involving edge-sharing tetrahedra gives rise to a four-atom ring in which Ge and Se atoms alternate. These rings are found to be quasiplanar, with an average sum of bond angles (357°) very close to the ideal value for the perfectly planar ring (360°). In these rings, the average Ge-Se-Ge angle amounts to 80.2° (Fig. 3). The corresponding Ge-Se bond length averages to 2.41 Å with a standard deviation of 0.025 Å. Thus, the bond lengths in the rings do not differ significantly from the mean Ge-Se bond length (2.42 Å).

TABLE II. Composition of first-neighbor shells of Ge and Se atoms expressed as a percentage in our models of v-$GeSe_2$. For each composition, the coordination is indicated by ℓ. For Ge-Se and Se-Se bonds, we used cutoff radii of 3.0 and 2.7 Å, respectively. Ge-Ge bonds do not occur in our models. We also quantify the amount of homopolar bonds and of edge-sharing tetrahedra (ES-T) in terms of percentages of the involved atoms. Experimental values are taken from Ref. 4.

Composition	ℓ	Model I	Model II	Model III	Expt.
			Ge		
Se_3	3	5	7	20	
Se_4	4	95	93	78	
Se_5	5			2	
			Se		
Ge	1	1		1	
SeGe	2	3	8	20	
Ge_2	2	92	86	55	
Se_2	2			4	
$SeGe_2$	3	2			
Se_2Ge	3		1		
Ge_3	3	2	5	20	
Se-Se		5	9	24	20
Ge-Ge					25
ES-T		33	15	48	34

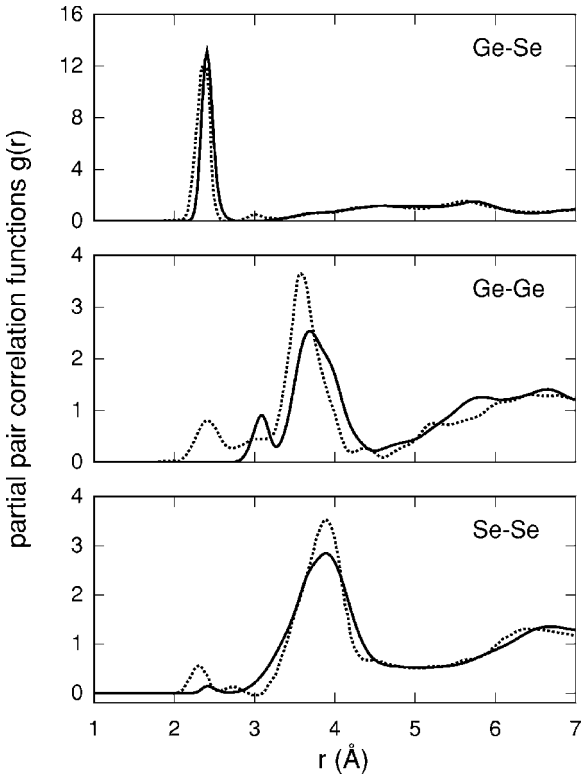

FIG. 4. Partial pair-correlation functions of v-$GeSe_2$ at room temperature: model I (solid) and experimental data from Ref. 4 (dotted).

The occurrence of homopolar bonds in v-$GeSe_2$ has been observed experimentally.[4,21] In model I, the Se-Se homopolar bonds involve 5% of the Se atoms (Table II), considerably less than found experimentally (20%).[4] This difference should be assigned to the classical molecular dynamics part of our generation procedure, which does not allow for the formation of such homopolar bonds. Model II similarly features a low fraction (9%). At variance, the *ab initio* generation scheme used for model III gives a fraction of 24%, only slightly larger than experiment. The Se-Se bond lengths are generally found to overestimate the experimental value by about 5% (~2.42 Å). Recent neutron-diffraction data indicate that 25% of the Ge atoms are involved in Ge-Ge homopolar bonds. However, none of our models shows such bonds. At present, this corresponds to a limitation of our model generation procedures. Vibrational features associated with Ge-Ge bonds can therefore not be identified with the present set of models.

We calculated pair-correlation functions (PCFs) using Gaussian correlations of which the spread is derived from vibrational eigenmodes and frequencies obtained in the harmonic approximation. A detailed account of this approach is given in Ref. 15. This formulation offers the advantage of accounting for the zero-point motion and has been found to give a good description of oxide glasses at 300 K.[36,37]

In Fig. 4, we show the PCFs calculated at room temperature for model I of v-$GeSe_2$ together with corresponding experimental data.[4] Overall, we register a good agreement between experiment and theory. In particular, the Ge-Se PCF is dominated by a strong peak in correspondence of the Ge-Se

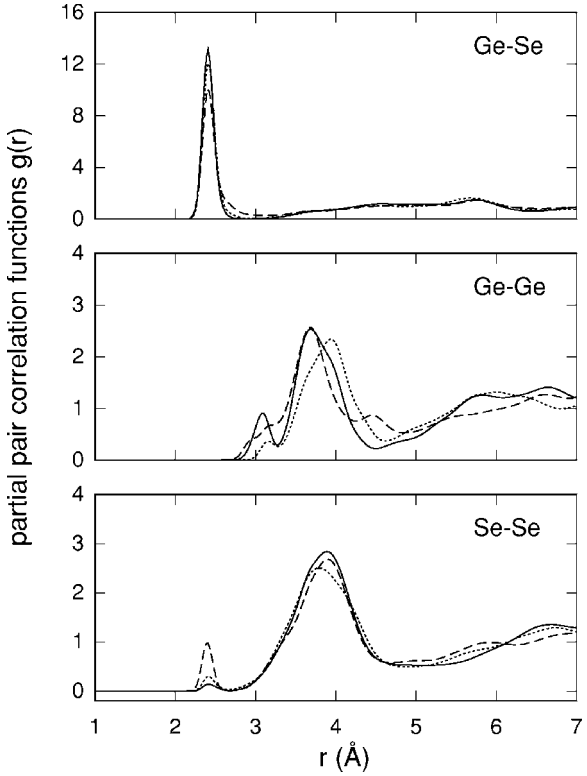

FIG. 5. Comparison between calculated partial pair-correlation functions for models I (solid), II (dotted), and III (dashed).

bond length. A spherical integration of the theoretical peak gives a coordination number of 3.96, slightly higher than the experimental value of 3.7.[4] The theoretical peak is shifted by ~0.06 Å with respect to the experimental one, reflecting the longer mean bond length in the simulation. Similarly, the main peak in the Ge-Ge PCF is shifted by ~0.1 Å with respect to the experimental peak. The first two peaks in the theoretical Ge-Ge PCF reflect the Ge-Se-Ge angle distribution (Fig. 3), distinguishing Ge-Ge correlations in edge- and corner-sharing tetrahedra at 3.1 and 4.0 Å, respectively. The experimental Ge-Ge PCF shows in addition a peak at 2.42 Å corresponding to homopolar Ge-Ge bonds, which are absent in our models. The difference between the experimental and theoretical Se-Se PCF is mainly limited to the peak at 2.32 Å corresponding to Se-Se homopolar bonds. Its intensity relates to the concentration of such bonds, which is lower in model I (5%) than in the experiment (20%) (Table II).

In Fig. 5, we compare the pair-correlation functions calculated for our three model structures. The Ge-Se PCF has a first prominent peak corresponding to the Ge-Se bond length. The three models only differ by the height of this peak (see Fig. 2 and Table I). The Ge-Ge PCF shows more significant differences among the models. The relative heights of the first two peaks reflect the number of edge- and corner-sharing tetrahedra in each model (Table II). For the Se-Se PCF, the three models give overall similar results. Significant differences are only observed for the intensity of the first peak, which scales according to the number of homopolar Se-Se bonds (Table II). Among the three models, model III shows the best agreement with experiment for this feature.

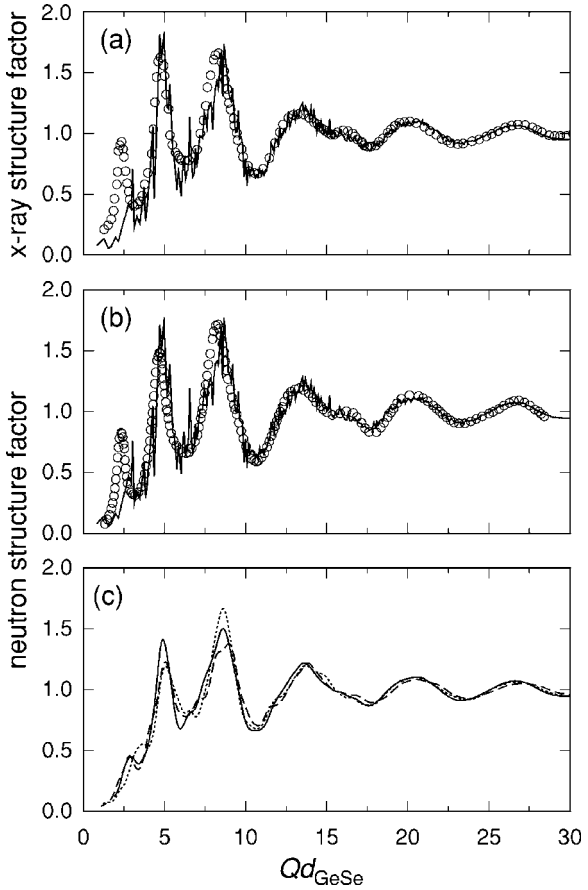

FIG. 6. (a) X-ray and (b) neutron structure factors at room temperature for model I (solid) compared to the experimental data (circles) obtained in Refs. 20 and 40, respectively. (c) Comparison between calculated neutron structure factors of models I (solid), II (dotted), and III (dashed). A Gaussian broadening of 0.1 $Å^{-1}$ is used. The bond lengths in Table I are used to rescale the transferred momenta.

B. Reciprocal-space properties

We calculated x-ray, neutron, and partial structure factors at room temperature accounting for the vibrations in the harmonic approximation.[15] For the x-ray structure factor, we used atomic structure factors dependent on the scattering vector.[38] For the neutron structure factor, we used scattering lengths of 8.185 and 7.97 fm for Ge and Se, respectively.[39] For v-$GeSe_2$, x-ray and neutron-diffraction probes give very similar structure factors, since Ge and Se atomic species have close atomic numbers and similar neutron-scattering lengths.

In Figs. 6(a) and 6(b), we show the comparison between the x-ray and neutron structure factors calculated for model I and the experimental data.[20,40] In the figure, the scattering vectors are rescaled to an adimensional quantity Qd_{GeSe}, in consideration of the different average bond lengths d_{GeSe} in theory and experiment. Our model structure shows good agreement with both experimental results, particularly in the range $Qd_{GeSe} \geqslant 7$, which mostly depends on the tetrahedral structural unit. The first sharp diffraction peak (FSDP) of model I also shows fair agreement with the experiment as far

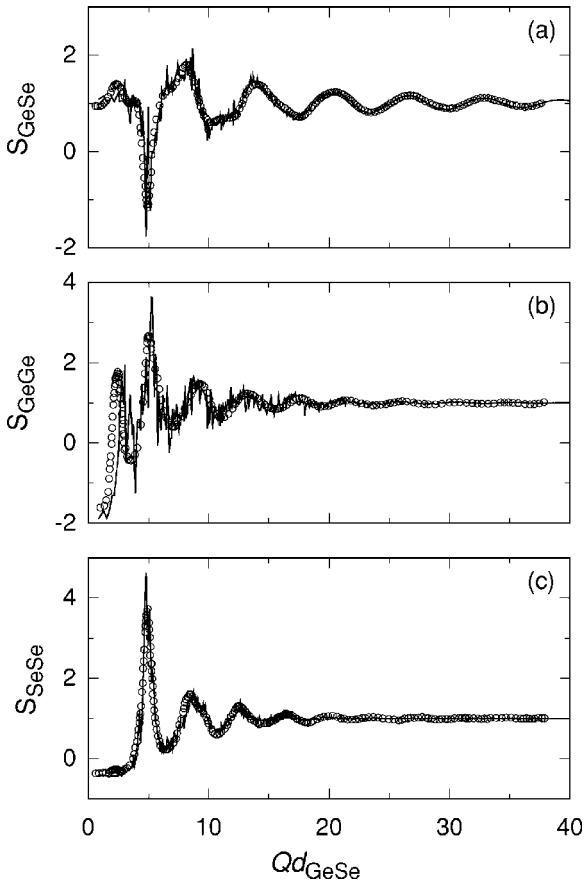

FIG. 7. Faber-Ziman partial structure factors at room temperature: model I (solid) vs experiment (Ref. 4) (circles). Transferred momenta are rescaled as in Fig. 6.

as its intensity is concerned, but its position is found to be shifted to larger scattering vectors. This shift originates in a nontrivial way from slight differences in the atomic arrangements occurring over intermediate-range lengths.[41,42]

We compare in Fig. 6(c) the neutron structure factors calculated for models I, II, and III. The comparison shows that the structure factors differ for $Qd_{GeSe} \leqslant 8$, but that they become very similar for larger Q vectors. Models I and III give very similar FSDPs as far as both their positions and intensities are concerned. In model II, the FSDP does not stand out clearly and appears as a shoulder of the peak at $Qd_{GeSe} = 5$.

The partial structure factors in the Faber-Ziman formulation calculated for model I are compared to their experimental counterparts[4] in Fig. 7. The agreement with experiment is excellent for the partial structure factors S_{GeSe} and S_{SeSe} over the full range of scattering vectors, including the FSDP region. For S_{GeGe}, the agreement is similarly very good in the range of scattering vectors beyond the FSDP. We record the largest differences between theory and experiment in the FSDP region of S_{GeGe}. These differences might result from the absence of homopolar Ge-Ge bonds in model I. A similar level of agreement is found for models II and III (not shown).

To highlight effects associated with the chemical order, we focus in Fig. 8 on the concentration-concentration structure factor S_{CC}, as defined in the Bhatia-Thornton formulation.[43] We note that the number-number structure factor S_{NN} in this formulation (not shown) faithfully reproduces the neutron structure factor because of the close scattering lengths of Ge and Se atoms.[5] In Fig. 8(a), we compare the S_{CC} of model I with experiment,[21] finding overall good agreement. In particular, in the FSDP region, the theoretical spectrum shows a feature of comparable intensity with respect to the experimental FSDP. The respective results for models I, II, and III are compared in Fig. 8(b). Despite the important structural differences between the models, their S_{CC} structure factors are very similar, with only minor discernable variations up to ~ 6 Å^{-1}.

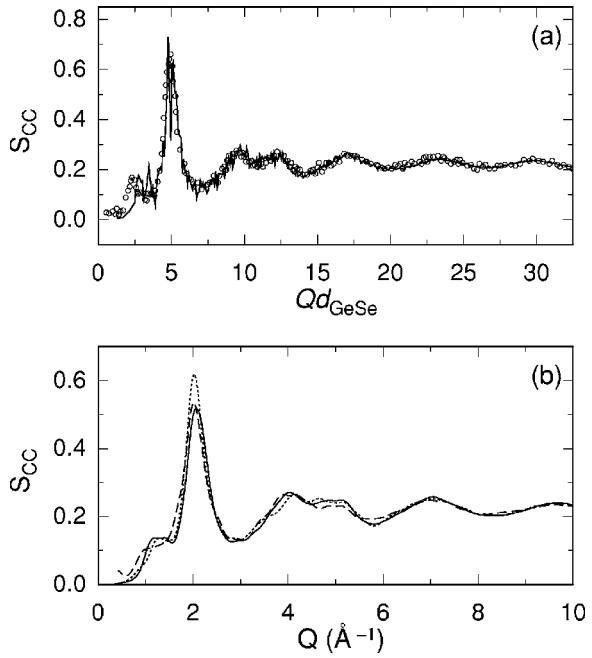

FIG. 8. (a) Bhatia-Thornton concentration-concentration partial structure factors at room temperature: model I (solid) vs experiment (Ref. 21) (circles). Transferred momenta are rescaled as in Fig. 6. (b) Comparison between calculated concentration-concentration partial structure factors of models I (solid), II (dotted), and III (dashed). A Gaussian broadening of 0.1 Å^{-1} is used.

Apart from the concentration of homopolar bonds, our three models well reproduce the experimental diffraction data pertaining to short-range order. This good agreement applies to models of both kinds of structural conception (models I and II vs model III), thereby confirming the weak sensitivity of diffraction probes to the underlying chemical order.

IV. VIBRATIONAL PROPERTIES

In Fig. 9, we compare the vibrational densities of states (v-DOSs) of models I, II, and III. The three spectra feature three main frequency bands: a low band extending up to 150 cm^{-1}, a middle band (150–200 cm^{-1}), and a high band above 200 cm^{-1}. Overall, the three models show similar spectra with minor differences. The model-dependent variations are larger for the middle and high bands than for the low band.

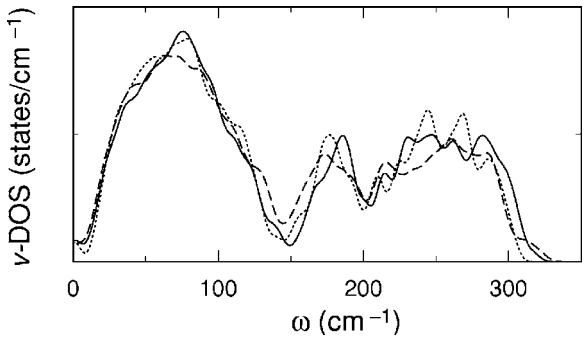

FIG. 9. Normalized vibrational density of states (v-DOS) of v-$GeSe_2$: a comparison between models I (solid), II (dotted), and III (dashed). A Gaussian broadening of 4 cm^{-1} is used.

To analyze the nature of the vibrational modes, we focus in the following on the v-DOS of model I. In Fig. 10(a), we show the decomposition of the v-DOS according to the Se and Ge weights in the vibrational eigenmodes. The low band shows a high Se character with a Se weight about three times larger than the Ge weight, a ratio higher than the ratio between the atomic concentrations. The dominance of Se character is even more important in the middle band, which features a weak Ge contribution. At variance the Ge character is well represented in the high band which shows similar Ge and Se weights. In Fig. 10(b), we further analyze the vibrations of the Se atoms in terms of rocking, bending, and stretching motions.[44] In this analysis, we only considered Se atoms twofold coordinated with Ge, which correspond to 94% of the Se atoms in model I. We took the bending direction along the bisector of Ge-Se-Ge angle, the rocking direction normal to the plane of the Ge-Se-Ge bridge, and the stretching direction orthogonal to the previous two. The projections on these directions show that rocking motions only contribute to the low band, whereas bending and stretching motions strongly intermix in the middle and high bands. In particular, the bending and stretching motions contribute with similar weights to the Se peak at ~180 cm^{-1}. The bending contribution shows a second peak at 285 cm^{-1}, while a second peak of the stretching contribution occurs at 225 cm^{-1}.

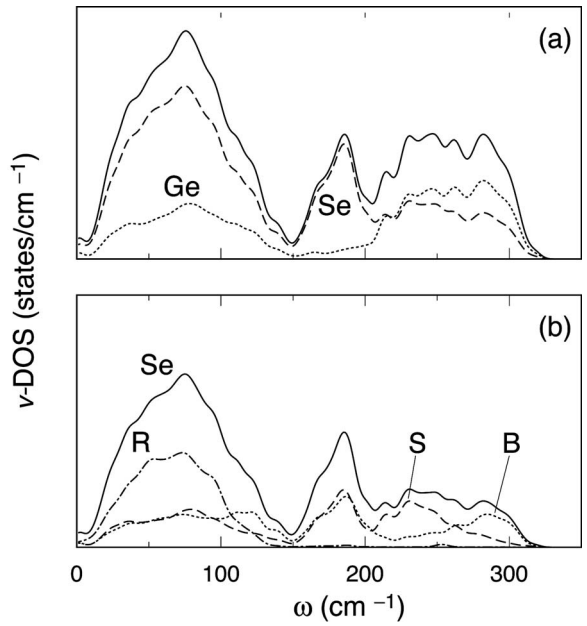

FIG. 10. (a) Vibrational density of states (v-DOS) of model I of v-$GeSe_2$ and its decomposition into Ge (dotted) and Se (dashed) weights. (b) Further decomposition of the Se weight into bending (dotted), rocking (dot-dashed), and stretching (dashed) motions. Only Se atoms twofold coordinated by Ge are considered. A Gaussian broadening of 4 cm^{-1} is used.

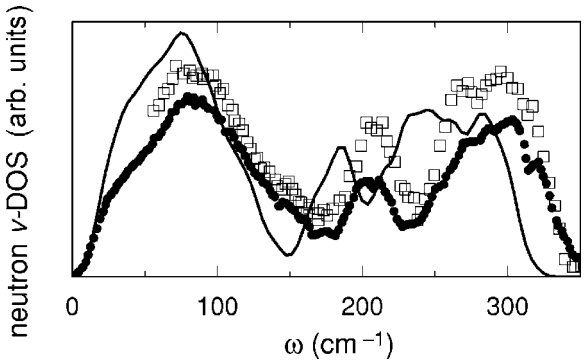

FIG. 11. Neutron vibrational density of states of v-$GeSe_2$ at 13 K calculated for model I (solid), compared to corresponding experimental data of Ref. 46 (open squares). Experimental data obtained at room temperature (Ref. 47, closed circles) are shown for comparison. Transferred momenta are taken in the range 0.6–8.5 $Å^{-1}$, corresponding to the experimental interval (Ref. 46).

A comparison with experiment can be carried out for the inelastic neutron spectrum. We calculated this spectrum for model I in the one-phonon approximation.[10,45] The calculated inelastic neutron spectrum in Fig. 11 is found to closely resemble the v-DOS in Fig. 9, in analogy with similar comparisons for v-SiO_2 (Ref. 10) and v-GeO_2 (Ref. 15). Figure 11 also shows that the calculated inelastic neutron spectrum compares well with the available experimental spectra,[46,47] reproducing all the salient features. However, the calculated frequencies are systematically lower than the measured ones. Such underestimations have already been encountered in previous theoretical work on disordered systems.[8,14] The good agreement with experiment recorded for the inelastic neutron spectrum appears as a solid basis for envisaging the analyses of the infrared and Raman spectra.

TABLE III. Average isotropic Born charges of all Se (Z^*_{Se}) and Ge (Z^*_{Ge}) atoms in our models of v-$GeSe_2$. The average isotropic Born charges of threefold coordinated Se (Z^*_{SeIII}) and Ge (Z^*_{GeIII}) atoms are also given. Standard deviations of the respective distributions are given in parentheses.

Model	Z^*_{SeIII}	Z^*_{GeIII}	Z^*_{Se}	Z^*_{Ge}
I	−1.67 (0.08)	2.18 (0.25)	−1.31 (0.40)	2.63 (0.21)
II	−1.93 (0.23)	2.43 (0.39)	−1.38 (0.57)	2.76 (0.29)
III	−1.84 (0.32)	2.46 (0.53)	−1.32 (0.60)	2.63 (0.39)
All	−1.84 (0.29)	2.39 (0.44)	−1.33 (0.51)	2.67 (0.30)

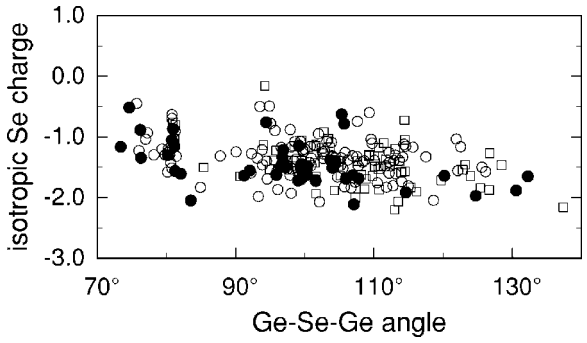

FIG. 12. Isotropic Se Born charge (Z^*_{Se}) vs Ge-Se-Ge angle for models I (open circles), II (open squares), and III (closed circles). Only Se atoms twofold coordinated by Ge are considered.

V. INFRARED SPECTRA

A. Born charge tensors

The coupling of the vibrational motions to the electric field is described by the dynamical Born charge tensors.[48] We calculated Born charge tensors Z^* of all the Ge and Se atoms in our models.

Because of the predominant tetrahedral bonding of the Ge atoms, the Born charge tensor of these atoms is well described by an isotropic tensor. Averaging over all the Ge atoms in our models, we obtained an isotropic Born charge of 2.67. Correspondingly, the average of the isotropic Born charge of the Se atoms is −1.33. The individual models give similar average isotropic Born charges, as summarized in Table III. It is interesting to note that the standard deviations of the distributions of isotropic Born charges in v-$GeSe_2$ are at least two times larger than in v-SiO_2 or v-GeO_2.[11,15]

Focusing on the Se atoms with two Ge nearest neighbors, the dynamical Born tensor is conveniently expressed with respect to a local reference set based on the orientation of the Ge-Se-Ge unit. We took the x, y, and z directions along the bending, rocking, and stretching directions defined in Sec. IV. By averaging over all models, we obtained

$$Z^*_{Se} = \begin{pmatrix} -0.96 & 0.02 & 0.05 \\ 0.01 & -1.00 & 0.00 \\ 0.04 & 0.04 & -2.25 \end{pmatrix}. \quad (1)$$

The average Z^*_{Se} tensor is well described by a diagonal tensor, as already found for the oxygen atoms in silica and germania.[11,15] The displacements along the stretching direction (z direction) couple to the electric field twice as much as those along the other directions. Typically, the Se Born charge along the z direction is 20% lower than the corresponding O one in disordered oxides.[15]

For the Se atoms with two Ge nearest neighbors, we investigated the dependence of the isotropic part (Z^*_{Se}) of the Se Born charge tensors on the Ge-Se-Ge angle. Our results in Fig. 12 show that Z^*_{Se} tends to decrease with increasing Ge-Se-Ge angle. Such a dependence on the angle was already observed for the oxygen isotropic charge in v-SiO_2 and v-GeO_2.[11,15] However, in v-$GeSe_2$, the Se isotropic Born charge is much less sensitive to the intertetrahedral angle and the spread is significantly larger.

We also considered the average isotropic Born charges of threefold coordinated Se (Z^*_{SeIII}) and Ge (Z^*_{GeIII}) atoms. From an average over the three models, we derived $Z^*_{SeIII}=-1.84$ and $Z^*_{GeIII}=2.39$. The value for the threefold coordinated Se atoms is more negative by 38% with respect to the full average, indicating a higher dynamic ionicity for these atoms. At variance, the threefold coordinated Ge atoms show a lower ionicity, as witnessed by a decrease of 10% of their isotropic Born charges. We note that the local environment around the threefold coordinated atoms differs not only because of the modified coordination but also because of their specific Ge-Se bond length (~2.6 Å), which, for both threefold coordinated Se and Ge atoms, is found to elongate by about 7% with respect to the average bond length (Table I). Average Born charges for threefold atoms in the individual models are given in Table III. For Se atoms forming homopolar bonds, we calculated an average isotropic Born charge of −0.56 with a spread of 0.72. The spread is significantly larger than typical values in Table III, indicating that these Born charges are highly sensitive to the local disorder.

TABLE IV. High-frequency (ϵ_∞) and static dielectric constants (ϵ_0) for our models of v-$GeSe_2$. Respective experimental data are taken from Refs. 49 and 50.

	Model I	Model II	Model III	Expt.
ϵ_∞	7.2	7.65	7.3	5.5
ϵ_0	11.4	14.1	15.0	7.22

B. Dielectric constants

For our models of v-$GeSe_2$, we calculated the high-frequency dielectric constant ϵ_∞ through second derivatives of the energy with respect to the electric field.[29,30] As given in Table IV, we calculated average values of ϵ_∞ in the range 7.2–7.7. Infrared oscillator strengths can be derived from the vibrational eigenmodes and the dynamical Born charges.[11,15] The static dielectric constants ϵ_0 are then obtained from the vibrational frequencies and their corresponding oscillator strengths.[11] The values calculated for our models range between 11 and 15 (Table IV).

The calculated values for both the high-frequency and static dielectric constants are larger than the corresponding experimental values of 5.5 (Ref. 49) and 7.2 (Ref. 50), respectively. The differences between theory and experiment are too large to be explained by the usual overestimations of DFT calculations.[51] To understand the origin of these differences, it is instructive to consider the high-temperature crystalline form of $GeSe_2$, which is composed of corner- and edge-sharing tetrahedra.[52] Measured values of ϵ_∞ and ϵ_0 for this structure give, after averaging over Cartesian directions, ~8.7 and ~10.5, respectively.[53] These values do not reconcile well with the experimental data for v-$GeSe_2$. However, they are consistent with the theoretical values for model I. Models II and III show considerably higher values for ϵ_0, indicating that this property is sensitive to the variety of

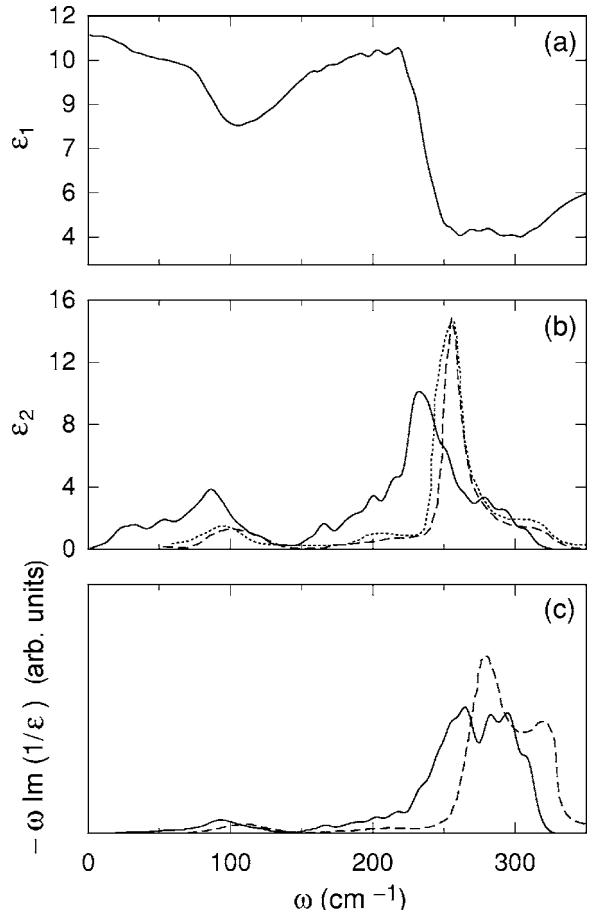

FIG. 13. Dielectric function of model I of v-$GeSe_2$ (solid) compared to experimental data from Ref. 55 (dotted) and Ref. 54 (dashed): (a) real part, (b) imaginary part, and (c) longitudinal response $-\omega\,\mathrm{Im}(1/\epsilon)$. A Lorentzian broadening of 8 cm^{-1} is used in (a), while Gaussian broadenings of 4 cm^{-1} are used in (b) and (c). In (c), the experimental and theoretical spectra are rescaled to show the same integrated intensity.

underlying atomic structures considered here for v-$GeSe_2$.

C. Dielectric functions

The high-frequency dielectric constant, the vibrational frequencies, and their corresponding oscillator strengths fully determine the dielectric function.[11,15] In Fig. 13, we give for model I the real (ϵ_1) and imaginary (ϵ_2) parts of the dielectric function, together with the longitudinal response function $-\omega\,\mathrm{Im}(1/\epsilon)$. Available experimental spectra from Refs. 54 and 55 are also reported for comparison.

The calculated ϵ_1 [Fig. 13(a)] shows two clear resonances in correspondence of the two principal peaks of ϵ_2 at 86 and 232 cm^{-1}. We did not find an experimental spectrum for ϵ_1 of v-$GeSe_2$. However, the calculated spectrum shows a similar shape as for v-SiO_2 and v-GeO_2,[15,30] with broadened features due to the higher degree of disorder.

For ϵ_2, our results reproduce the two main peaks of the experimental spectrum [Fig. 13(b)].[54,55] As for the v-DOS (Fig. 11), the peak positions in the theoretical spectrum are found to be shifted to lower frequencies with respect to their positions in the experimental spectrum, by 10 and 25 cm^{-1} for the peaks at 86 and 232 cm^{-1}, respectively. The peaks in the calculated spectrum are broader than their experimental counterparts. We attribute this effect to an excessive degree of residual strain in our model structure.[30]

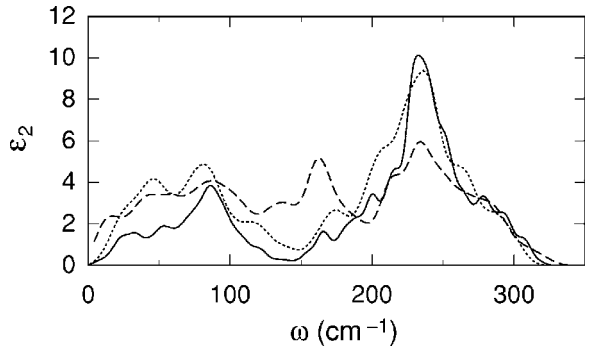

FIG. 14. Comparison between the calculated imaginary parts of the dielectric functions of v-$GeSe_2$ for models I (solid), II (dotted), and III (dashed). A Gaussian broadening of 4 cm^{-1} is used.

The theoretical longitudinal response function $-\omega\,\mathrm{Im}(1/\epsilon)$ shows fair agreement with the corresponding experimental spectrum[54] [Fig. 13(c)] as far as the global shape and the relative heights of the main features are concerned. The shifts of the main features with respect to their position in ϵ_2 give the longitudinal-optic–transverse-optic (LO-TO) splittings. We obtained LO-TO splittings of 7 and 33 cm^{-1} for the two main features in ϵ_2 in fair agreement with the corresponding experimental splittings of 10 and 24 cm^{-1}.

In Fig. 14, we compare the imaginary parts of the dielectric functions calculated for our three models. The agreement with experiment is clearly best for model I, and degrades going from model I to model III. The spectrum of model II resembles that of model I, but the main features are further broadened. Indeed, these two models both show a large predominance of tetrahedra, but structural distortions are clearly more important in model II, as witnessed by the larger spreads in the bond-length and Se-Ge-Se angle distributions (Table I). For model III, the broadening increases further and an additional peak arises at $\sim$160 cm^{-1} which does not occur in the experiment. The degree of disorder in the first coordination shells in this model appears therefore incompatible with the experimental shape of the infrared ϵ_2.

VI. RAMAN SPECTRA

Raman spectra of v-$GeSe_2$ are usually obtained for incoming and outgoing photons with either parallel (HH) or perpendicular polarizations (HV). The experimental HH Raman spectrum of v-$GeSe_2$ is characterized by a strong doublet with a principal peak located at 201 cm^{-1} and a companion peak at 218 cm^{-1}.[18] Investigating Ge_xSe_{1-x} samples for varying x, Tronc *et al.*[56] noticed that the principal line shows up as soon as a finite concentration of Ge occurs, and that its intensity strongly increases with Ge content. Therefore, the principal line indicates the occurrence of Ge atoms in a Se environment, i.e., the formation of the $Ge(Se_{1/2})_4$ tetrahedron. The origin of the companion line has long been

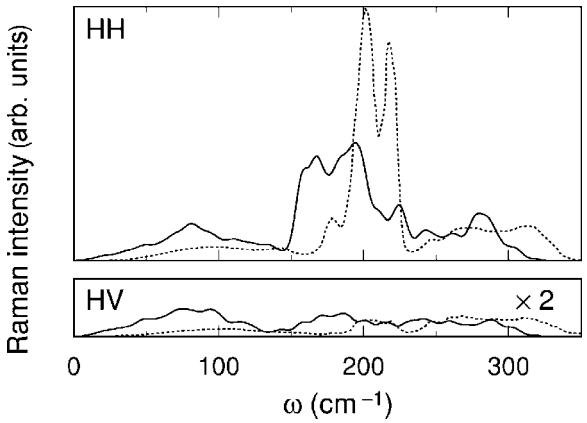

FIG. 15. Reduced HH and HV Raman spectra of v-$GeSe_2$ for model I of v-$GeSe_2$ (solid), compared to experimental data of Ref. 54 (dotted). The calculated HH spectrum is scaled to match the integrated intensity of the experimental spectrum. The same scaling factor is used for the theoretical HV spectrum. For clarity, the HV spectra are magnified by a factor of 2. A Gaussian broadening of 4 cm^{-1} is used.

debated.[17–19,57] Recent work supports the assignment of this line to vibrations in edge-sharing tetrahedra.[17–19] The high-temperature crystalline form of $GeSe_2$ which contains edge-sharing tetrahedra indeed shows a line at 213 cm^{-1}, in close correspondence with the companion line of v-$GeSe_2$.

Other minor features can be discerned in the HH Raman spectrum of v-$GeSe_2$. The features located at 240 and 270 cm^{-1} are generally interpreted as due to vibrations associated with the Se-Se homopolar bonds.[18,56] This assignment is achieved through comparisons with the Raman spectra of amorphous and crystalline selenium. The shoulder at $\sim$179 cm^{-1} on the low-frequency side of the principal peak has been assigned to the homopolar Ge-Ge bond in an ethanelike atomic structure embedded in the glass.[19]

A. Comparison with experiment

In Fig. 15, we compare the HH and HV reduced Raman spectra calculated for model I to the experimental spectra.[54] In the theoretical HH spectrum, the doublet is clearly recognizable despite the larger widths of the peaks and the overall shift to lower frequencies compared to the experiment. The calculated spectrum also shows bands of comparable intensity to the experimental spectrum, at lower and higher frequencies. The Raman intensity of the HV spectrum is considerably weaker than that of the HH spectrum. We note that the experimental ratio between the integrated intensities of the HH and HV spectra is fairly well reproduced by our calculation. The experimental HV spectrum shows three distinct bands. In the calculation, the lowest band is clearly distinguishable but the two higher bands are found to merge.

In Fig. 16, we show the reduced HH Raman spectra of models I, II, and III. Among these three models, the best agreement with the experimental spectrum is found for model I (Fig. 15). The principal feature in the spectrum of model II occurs in correspondence of the central doublet. However, the bands at lower and higher frequencies feature a considerably higher intensity than in model I. This results in a diminished contrast between the intensities in the central region of the spectrum and in the sidebands. The spectrum of model III shows a highly fluctuating intensity and differs significantly from the experimental spectrum. The calculated intensities are on average three times larger than in model I, indicating a higher degree of polarizability in model III. The absence of any similarity with the experimental spectrum and the high polarizability suggests that the variety of bonding motifs in model III does not give a reliable representation of the structure of v-$GeSe_2$.

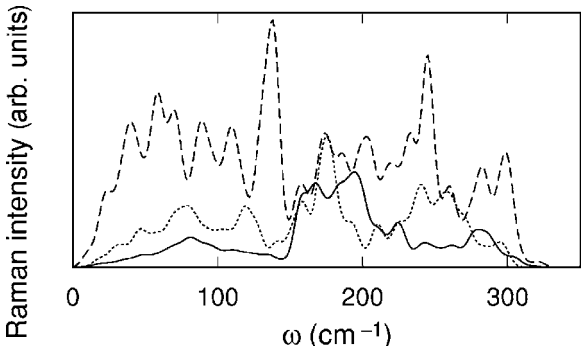

FIG. 16. Comparison between the calculated reduced HH Raman spectra of v-$GeSe_2$ for models I (solid), II (dotted), and III (dashed). A Gaussian broadening of 4 cm^{-1} is used.

The three models showed comparable structure factors [Figs. 6(c) and 8(b)] and vibrational densities of states (Fig. 9). Nevertheless, we note that important differences occur in their Raman spectra. This indicates that the sensitivity of Raman coupling factors on structural parameters is particularly high. Therefore, the agreement between calculated and measured Raman spectra is a selective criterion for identifying an optimal model structure.

B. Analysis in terms of atomic vibrations

With respect to their experimental counterparts, the simulated Raman spectra offer the advantage that they can conveniently be analyzed in terms of the underlying vibrational modes. In the following, we focused on model I, which shows the best agreement with experiment. Figure 17(a) gives the decomposition of the Raman spectrum into Se and Ge weights. This decomposition is achieved by selecting the components of the vibrational eigenmodes specific to either Se or Ge prior to the calculation of the Raman intensities. While the components obtained in this way do not sum up to give the full spectrum because of the interference terms, this analysis nevertheless provides insight into the origin of the various features. The central band (145–225 cm^{-1}) appears to originate almost exclusively from Se motions, whereas the rest of the spectrum also shows a considerable contribution from Ge vibrations. Overall, the distributions of the Se and Ge weights in the HH Raman spectrum show a similar behavior as in the vibrational density of states.

The contribution of Se atoms is further analyzed in Fig. 17(b) in terms of rocking, bending, and stretching motions. For this analysis, the decomposition shows important differ-

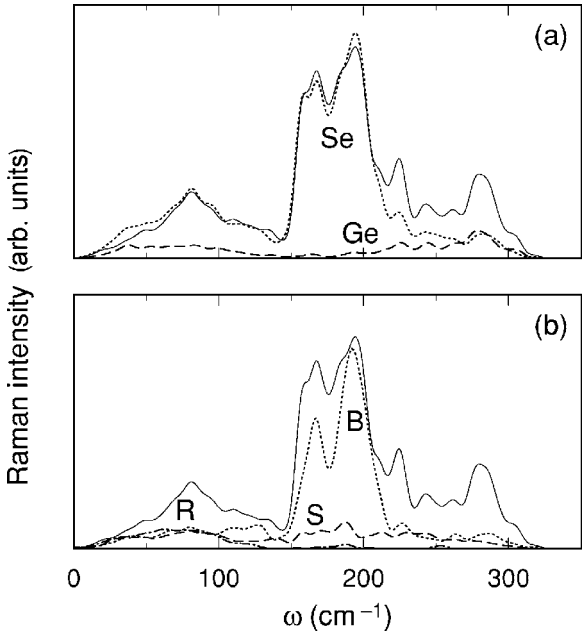

FIG. 17. (a) Decomposition of the reduced HH Raman spectrum of model I (solid) into Se (dotted) and Ge (dashed) weights following the procedure described in the text. (b) Further decomposition of the Se weight into rocking (dot-dashed), bending (dotted), and stretching (dashed) contributions (see text). A Gaussian broadening of 4 cm^{-1} is used.

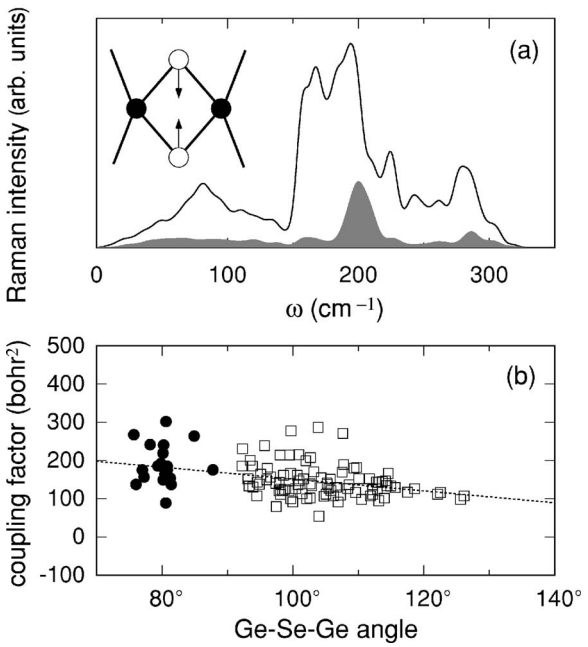

FIG. 18. (a) Raman intensity (shaded) associated with in-phase Se bending vibrations in four-atom rings (see inset), compared to the full reduced HH Raman spectrum of model I of v-$GeSe_2$ (solid). A Gaussian broadening of 4 cm^{-1} is used. (b) Isotropic coupling factor for Se bending motions vs Ge-Se-Ge angle for Se atoms in model I. Only Se atoms twofold coordinated by Ge are considered, either inside (closed circles) or outside (open squares) of four-atom rings. The dotted line corresponds to a linear fit of the data.

ences with respect to the analogous one of the vibrational density of states. In the frequency region below the main doublet, the Raman intensities associated with rocking, bending, and stretching motions have similar weights, while the rocking motions dominate in the v-DOS. Although the v-DOS indicates that both stretching and bending motions occur in comparable amounts in the frequency range of the main doublet, the major contribution to the Raman intensity of this feature originates mainly from the latter ones. The sum of the stretching and bending contributions to the principal peak noticeably differs from its total Se weight, indicating the occurrence of interference terms. For larger frequencies, both the contributions of stretching and bending motions are found to be of similar intensity, but do not separate in distinct peaks as for the v-DOS. In particular, the feature at 280 cm^{-1}, which corresponds to the experimental peak at 310 cm^{-1} (Ref. 18), shows the highest fraction of Ge motion and is accompanied by both stretching and bending Se motions.

This analysis shows that the bending motions give the largest contribution to the doublet in the HH Raman spectrum of v-$GeSe_2$. As for v-SiO_2 (Refs. 13 and 58) and v-GeO_2 (Refs. 14 and 15), the coupling to the bending motions is mainly isotropic. In particular, in the region of the main doublet, the isotropic bending contribution of Se atoms twofold coordinated by Ge accounts for 65% of the integrated intensity. In v-SiO_2 and v-GeO_2, the contribution of the isotropic bending coupling to O atoms reached percentages as high as 90% in the region of the principal Raman features.[13,14] In v-$GeSe_2$, this percentage is lower because of the nonvanishing weight associated with stretching Se motions, particularly for the principal line.

C. Origin of the companion line

To investigate the contribution of edge-sharing tetrahedra to the HH Raman spectrum, we projected the vibrational eigenmodes onto Se breathing motions in four-atom rings. In these motions, the two Se atoms in the ring give rise to in-phase bending vibrations along the bisectors of their respective Ge-Se-Ge units.[17,18] We then determined the contribution of these ring vibrations to the spectrum by using the projected eigenmodes in the expression for the Raman intensities.[13,15] For model I, the Raman projection obtained in this way gives a distinct peak centered at 198 cm^{-1} [Fig. 18(a)], corresponding to the position of the companion line.[18] However, we note that the intensity associated with the projected eigenmodes does not account for the full intensity of this line. Since the vibrational motions in this frequency range are almost exclusively given by Se bending motions (Fig. 17), this result implies that the vibrational eigenmodes associated with four-atom ring vibrations are only partially localized on the rings. Analysis of models II and III gives a similar picture with projected peaks at 193 and 194 cm^{-1}, respectively (not shown).

In principle, the ratio between the intensities of the companion and principal lines provides information concerning the concentration of edge-sharing tetrahedra. The large widths of the doublet lines in our calculation prevent an accurate determination of this ratio. However, we note that the relation between the intensities of the two doublet lines and the concentrations of edge- and corner-sharing tetrahedra is

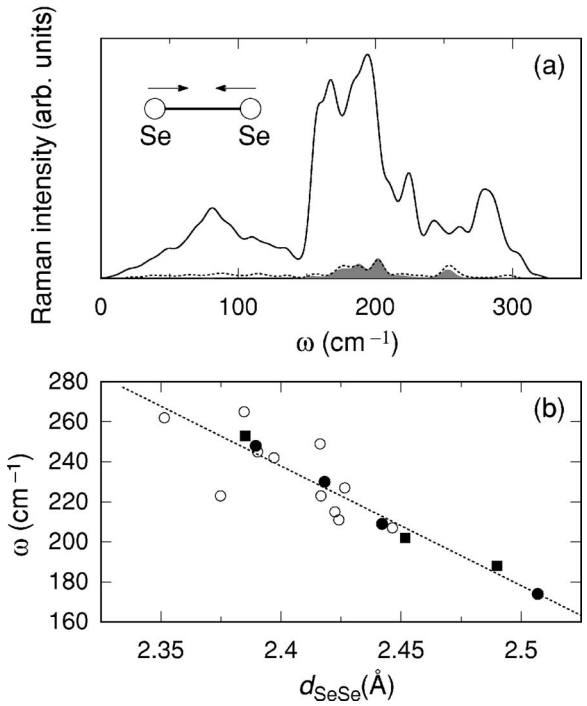

FIG. 19. (a) Raman intensities associated with homopolar bonded Se atoms (dotted) and in particular to their Se-Se stretching vibrations (shaded), compared to the full reduced HH Raman spectrum of model I of v-$GeSe_2$ (solid). A Gaussian broadening of 4 cm^{-1} is used. (b) Se-Se stretching-mode frequency vs bond-length d_{SeSe} for models I (closed circles), II (closed squares), and III (open circles). The dotted line corresponds to a linear fit of all the data.

not trivial. Such a relation should account for the fact that the principal and companion lines show different decompositions into bending and stretching Se motions, hence implying different Raman activities. To illustrate the dependence of the Raman coupling on structural properties, we focus on Se bending motions.[13,15] Figure 18(b) gives the isotropic component of this coupling vs Ge-Se-Ge bond angle. We observe that there is a considerable spread (50 $bohr^2$) in the calculated values. However, the average coupling factor for Se atoms in four-atom rings (190 $bohr^2$) is sensibly higher than the average value pertaining to the other Se atoms (144 $bohr^2$). Incidentally, we remark that these coupling factors are 1 order of magnitude larger than corresponding ones for v-SiO_2 and v-GeO_2. This directly affects the relative integrated Raman intensities of these glasses.

D. Raman signature of Se-Se bonds

With the intent of identifying Raman peaks associated with homopolar Se-Se bonds, we calculated the Raman intensities accounting only for the contribution of the atoms involved in these bonds. As shown in Fig. 19(a), this gives a Raman intensity which spans the entire range of the spectrum. Specific projection onto Se-Se bond stretching motions reduces the interval of the associated Raman intensity to 160–260 cm^{-1}. To understand this behavior, we then considered Se-Se bonds in an individual manner. We first projected the eigenmodes on the stretching motions associated with a given Se-Se bond, and then calculated the associated Raman intensity. For each Se-Se bond, this gave a sharp peak identifying a given frequency (not shown). In Fig. 19(b), the frequencies obtained in this way are displayed vs the corresponding bond lengths, revealing a linear trend. The relation is particularly well satisfied in models I and II, while model III shows larger deviations due to the higher level of disorder.

As can be inferred from the Se-Se partial pair-correlation functions in Fig. 4, the width of the Se-Se bond-length distribution in model I is comparable to the experimental result.[4] In view of the relation in Fig. 19(b), this further confirms that the contribution of Se-Se homopolar bonds to the HH Raman spectrum is spread over a large interval. To understand the extent of the observed Se-Se bond lengths in our models, we attempted to distinguish them according to their nearest-neighbor coordination, but could not find any specific relation. Our results would therefore suggest that assignments of specific features to Se-Se stretching motions are doubtful. However, we estimate that a definite conclusion can only be reached through the consideration of a statistically larger set of data.

VII. CONCLUSIONS

We studied the structural and vibrational properties of v-$GeSe_2$ within a density-functional scheme. In particular, we addressed the degree of chemical order in this vitreous material through the consideration of different model structures. Our investigation aimed at increasing our understanding of the structure of v-$GeSe_2$ by discriminating among the models through a comparison with experiment. We showed that diffraction probes are not sufficiently selective. The same observation also holds for the neutron vibrational density of states, which all models reproduce reasonably well. Significant differences among the model structures are observed for the infrared and Raman spectra. Comparison with experiment finally favors a structural model of v-$GeSe_2$ with strong chemical order.

Our best structural model shows a fair agreement with experiment for the infrared and Raman spectra. However, there appears to be significant room for further improvement. In particular, larger structural models appear instrumental to achieve this goal. Indeed, the finite-size effects affecting the level of distortion of the tetrahedra would be reduced, and consequently the quality of the infrared and Raman spectra would improve. Furthermore, larger statistics are needed to reliably represent spectral features associated with minority atomic arrangements.

An analysis which includes the vibrational spectra has now been applied to the series of tetrahedrally bonded glasses comprising v-SiO_2 (Refs. 11, 12, and 30), v-GeO_2 (Refs. 14 and 15), and v-$GeSe_2$. The former two glasses feature a network of corner-sharing tetrahedra and differ by their packing density. Therefore, structural models of these two oxide glasses generally differ by their distributions of intertetrahedral angles. The present study indicates that the structure of v-$GeSe_2$ is also predominantly given by tetrahedra. Differences with respect to the former oxide glasses con-

sist in the occurrence of edge-sharing tetrahedra and a low fraction of homopolar bonds. It is interesting to discuss how the structural differences between the networks of these three glasses affect the infrared and Raman spectra. The consideration of various models of v-SiO_2 and v-GeO_2 differing by the distributions of intertetrahedral angles led to minor differences in the infrared spectra. This should be contrasted with the important differences appearing in the infrared spectra of our models of v-$GeSe_2$, which show significant variations in the first-neighbor coordination shells. The sensitivity of Raman spectra on structural parameters, in particular, on the intertetrahedral bond-angle distribution, was already emphasized for v-SiO_2 and v-GeO_2. The strong sensitivity of Raman spectra on structural properties is confirmed for the models of v-$GeSe_2$, which show more significant structural variations than bond-angle distributions. Overall, the modeling of vibrational spectra has proved to be a sensitive tool for refining our understanding of atomic arrangements in disordered materials. In particular, these spectra allow us to clearly discriminate among structural models, which are barely distinguishable on the basis of diffraction data.

ACKNOWLEDGMENTS

We thank P. Umari for several useful discussions. Support from the Swiss National Science Foundation is acknowledged (Grant No. 200021-103562/1). The calculations were performed on the cluster PLEIADES of EPFL and on the computational facilities of DIT-EPFL, CSEA-EPFL, and the Swiss Center for Scientific Computing.

[1] *Insulating and Semiconducting Glasses*, edited by P. Boolchand (World Scientific, Singapore, 2000), Vol. 17.
[2] S. R. Elliott, *Physics of Amorphous Materials*, 2nd ed. (Longmans, London, 1990).
[3] P. Vashishta, R. K. Kalia, G. A. Antonio, and I. Ebbsjö, Phys. Rev. Lett. **62**, 1651 (1989); P. Vashishta, R. K. Kalia, and I. Ebbsjö, Phys. Rev. B **39**, 6034 (1989).
[4] I. Petri, P. S. Salmon, and H. E. Fischer, Phys. Rev. Lett. **84**, 2413 (2000).
[5] C. Massobrio, A. Pasquarello, and R. Car, Phys. Rev. Lett. **80**, 2342 (1998).
[6] C. Massobrio, A. Pasquarello, and R. Car, Phys. Rev. B **64**, 144205 (2001).
[7] M. Cobb and D. A. Drabold, Phys. Rev. B **56**, 3054 (1997).
[8] M. Cobb, D. A. Drabold, and R. L. Cappelletti, Phys. Rev. B **54**, 12162 (1996).
[9] P. Biswas, D. N. Tafen, and D. A. Drabold, Phys. Rev. B **71**, 054204 (2005).
[10] J. Sarnthein, A. Pasquarello, and R. Car, Science **275**, 1925 (1997); A. Pasquarello, J. Sarnthein, and R. Car, Phys. Rev. B **57**, 14133 (1998).
[11] A. Pasquarello and R. Car, Phys. Rev. Lett. **79**, 1766 (1997).
[12] A. Pasquarello and R. Car, Phys. Rev. Lett. **80**, 5145 (1998).
[13] P. Umari, X. Gonze, and A. Pasquarello, Phys. Rev. Lett. **90**, 027401 (2003).
[14] L. Giacomazzi, P. Umari, and A. Pasquarello, Phys. Rev. Lett. **95**, 075505 (2005).
[15] L. Giacomazzi, P. Umari, and A. Pasquarello, Phys. Rev. B **74**, 155208 (2006).
[16] P. Umari and A. Pasquarello, Phys. Rev. Lett. **95**, 137401 (2005).
[17] R. J. Nemanich, F. L. Galeener, J. C. Mikkelsen, Jr., G. A. N. Connell, G. Etherington, A. C. Wright, and R. N. Sinclair, Physica B & C **117&118B**, 959 (1983); R. J. Nemanich, S. A. Solin, and G. Lucovsky, Solid State Commun. **21**, 273 (1977).
[18] S. Sugai, Phys. Rev. B **35**, 1345 (1987).
[19] K. Jackson, A. Briley, S. Grossman, D. V. Porezag, and M. R. Pederson, Phys. Rev. B **60**, R14985 (1999).
[20] Q. Mei, C. J. Benmore, R. T. Hart, E. Bychkov, P. S. Salmon, C. D. Martin, F. M. Michel, S. M. Antao, P. J. Chupas, P. L. Lee, S. D. Shastri, J. B. Parise, K. Leinenweber, S. Amin, and J. L. Yarger, Phys. Rev. B **74**, 014203 (2006).
[21] P. S. Salmon and I. Petri, J. Phys.: Condens. Matter **15**, S1509 (2003).
[22] A. C. Wright, G. Etherington, J. A. E. Desa, R. N. Sinclair, G. A. N. Connell, and J. C. Mikkelsen, Jr., J. Non-Cryst. Solids **49**, 63 (1982).
[23] S. Nosé, Mol. Phys. **52**, 255 (1984); W. G. Hoover, Phys. Rev. A **31**, 1695 (1985).
[24] R. Car and M. Parrinello, Phys. Rev. Lett. **55**, 2471 (1985).
[25] A. Pasquarello, K. Laasonen, R. Car, C. Y. Lee, and D. Vanderbilt, Phys. Rev. Lett. **69**, 1982 (1992); K. Laasonen, A. Pasquarello, R. Car, C. Y. Lee, and D. Vanderbilt, Phys. Rev. B **47**, 10142 (1993).
[26] http://www.quantum-espresso.org
[27] J. P. Perdew, J. A. Chevary, S. H. Vosko, K. A. Jackson, M. R. Pederson, D. J. Singh, and C. Fiolhais, Phys. Rev. B **46**, 6671 (1992).
[28] A. Dal Corso, A. Pasquarello, A. Baldereschi, and R. Car, Phys. Rev. B **53**, 1180 (1996).
[29] P. Umari and A. Pasquarello, Phys. Rev. Lett. **89**, 157602 (2002).
[30] P. Umari and A. Pasquarello, Diamond Relat. Mater. **14**, 1255 (2005).
[31] K. Hachiya, J. Non-Cryst. Solids **291**, 160 (2001).
[32] N. Binggeli, N. Troullier, J. L. Martins, and J. R. Chelikowsky, Phys. Rev. B **44**, 4771 (1991); F. Giustino and A. Pasquarello, Phys. Rev. Lett. **96**, 216403 (2006).
[33] K. M. Kandil, M. F. Kotkata, M. L. Theye, A. Gheorghiu, C. Senemaud, and J. Dixmier, Phys. Rev. B **51**, 17565 (1995).
[34] D. J. Thouless, Phys. Rep., Phys. Lett. **13C**, 93 (1974).
[35] J. Sarnthein, A. Pasquarello, and R. Car, Phys. Rev. Lett. **74**, 4682 (1995); Phys. Rev. B **52**, 12690 (1995).
[36] A. Pasquarello, Phys. Rev. B **61**, 3951 (2000).
[37] S. Scandolo, P. Giannozzi, C. Cavazzoni, S. de Gironcoli, A. Pasquarello, and S. Baroni, Z. Kristallogr. **220**, 574 (2005).
[38] *International Tables for Crystallography* (Kluwer, Dordrecht, 1992), Vol. C, Table 6.1.1.4, pp. 500–502.
[39] Neutron-scattering lengths and cross sections are taken from http://www.ncnr.nist.gov/resources/n-lengths/
[40] S. Susman, K. J. Volin, D. G. Montague, and D. L. Price, J. Non-Cryst. Solids **125**, 168 (1990).

[41] S. R. Elliott, Phys. Rev. Lett. **67**, 711 (1991).
[42] C. Massobrio and A. Pasquarello, J. Chem. Phys. **114**, 7976 (2001); C. Massobrio, A. Pasquarello, and R. Car, J. Am. Chem. Soc. **121**, 2943 (1999).
[43] A. B. Bhatia and D. E. Thornton, Phys. Rev. B **2**, 3004 (1970).
[44] R. J. Bell, P. Dean, and D. C. Hibbins-Butler, J. Phys. C **4**, 1214 (1971).
[45] D. L. Price and J. M. Carpenter, J. Non-Cryst. Solids **92**, 153 (1987).
[46] U. Walter, D. L. Price, S. Susman, and K. J. Volin, Phys. Rev. B **37**, 4232 (1988).
[47] R. L. Cappelletti, M. Cobb, D. A. Drabold, and W. A. Kamitakahara, Phys. Rev. B **52**, 9133 (1995).
[48] R. Resta, Rev. Mod. Phys. **66**, 899 (1994).
[49] G. Lucovsky, Phys. Rev. B **15**, 5762 (1977).
[50] A. Feltz, H. Aust, and A. Blayer, J. Non-Cryst. Solids **55**, 179 (1983).
[51] X. Gonze, P. Ghosez, and R. W. Godby, Phys. Rev. Lett. **74**, 4035 (1995).
[52] G. Dittmar and H. Schäfer, Acta Crystallogr., Sect. B: Struct. Crystallogr. Cryst. Chem. **32**, 2726 (1976).
[53] Z. V. Popović and P. M. Nikolić, Solid State Commun. **27**, 561 (1978).
[54] K. Murase, in *Insulating and Semiconducting Glasses* (Ref. 1), pp. 415–463.
[55] G. Lucovsky, R. J. Nemanich, S. A. Solin, and R. C. Keezer, Solid State Commun. **17**, 1567 (1975).
[56] P. Tronc, M. Bensoussan, A. Brenac, and C. Sebenne, Phys. Rev. B **8**, 5947 (1973).
[57] P. M. Bridenbaugh, G. P. Espinosa, J. E. Griffiths, J. C. Phillips, and J. P. Remeika, Phys. Rev. B **20**, 4140 (1979).
[58] P. Umari and A. Pasquarello, J. Phys.: Condens. Matter **15**, S1547 (2003).